Supporting Information

Solid-State Photoisomerization Activating Topology-Mediated Photoluminescence in a Two-Dimensional Woven Polymer

Jiawei Duan[a,b], Zhengbo Zhong[a,b,c], Yuhao Mi[a,b], Pengyu Guo[a,b], Zihe Xu[a,b], Junwei Zhang[a,b], Zhangkai Chen[a], Tianhui Ren[a,c], Zhipeng Li*[a,b]

[a] State Key Laboratory of Synergistic Chem-Bio Synthesis, School of Chemistry and Chemical Engineering, Shanghai Jiao Tong University, Shanghai 200240, China.

[b] Key Laboratory of Intelligent Creation for Extreme Energy Materials, Ministry of Education, Shanghai Jiao Tong University, Shanghai 200240, China.

[c] Shaoxing Research Institute of Renewable Energy and Molecular Engineering, Shanghai Jiao Tong University, Shaoxing 312000, China.

Corresponding author: li_zp1314@sjtu.edu.cn (Z. Li)

Contents

1. Experimental Section

Synthesis of 1,4-bis(benzodioxa-borole)benzene (BDBB)

BDBB was prepared according to previous work[1]. In detail, a benzene-1,4-diboronic acid (0.26 g, 1.57 mmol) and catechol (0.35 g, 3.18 mmol) were placed into a 250 mL flask containing 100 mL toluene and 10 mL methanol. The solution was stirred and heated at 135 ℃ for 2 h with a Dean-Stark trap filled half full with 3 Å sieves. After the reaction solution cooled down, a white solid precipitated out. The solution was evaporated to dryness, and excess catechol was removed at 80 °C under reduced pressure. The resulting product took the form of white crystals (0.30 g, yield of 93.75%).

Preparation of 2DWP

2DWP crystals were synthesized via a modified solvothermal reaction, building upon the previous work[2]. In contrast to conventional solvothermal methods, a modified synthetic protocol emphasizing slow solvent evaporation was developed to grow two-dimensional woven polymer single crystals. Specifically, stoichiometric amounts of 1,2-bis(4-pyridyl)ethylene (**BPE**) (15.1 mg, 0.083 mmol) and **BDBB** (16.9 mg, 0.083 mmol) were dissolved in toluene (15 mL) by sonication. The sealed reaction mixture was heated to 90 °C for 24 hours, yielding a clear solution. Crystal growth was then initiated by slowly cooling the solution to 50 °C, followed by uncovered slow evaporation of the solvent for 12 hours, ultimately yielding orange-yellow crystals suitable for single-crystal X-ray diffraction analysis.

Structure Characterization

The single crystal of **2DWP** was determined at 213 K by a Bruker D8 VENTURE diffractometer equipped with a graphite monochromator, a charge-coupled device area detector, and copper Kα radiation (λ = 1.54184 Å). Powder X-ray diffraction (PXRD) was tested on a Bruker D8 ADVAANCE X-ray Diffractometer System with Cu Kα radiation at an angle of diffraction ranging from 5° to 35° with a specific scanning rate (5° min^{-1}). ^{1}H NMR spectra were recorded on a Bruker AVANCE III HD 500-MHz spectrometer. Fourier transform infrared spectroscopy (FT-IR) spectra were obtained (400–4000 cm^{-1} region) using the KBr pellet method on a PerkinElmer Spectrum 100. Scanning electron microscope (SEM) measurement was performed on a FEI Nova NanoSEM 450. UV-Vis diffuse reflectance spectroscopy (UV-Vis DRS) was measured using a HITACHI U-4100 UV-Vis-NIR spectrophotometer. Fluorescence (FL) spectra were collected using a PerkinElmer LS 55 FL spectrophotometer in the spectral range of 220–650 nm with excitation and emission slit of 15 nm.

Optical Spectroscopy Characterization.

Spectroscopic characterization was conducted in a confocal micro-PL system. A 405 nm CW laser coupled with a halogen lamp was employed for exciting molecular switching and in-situ tests, while 532 nm and 633 nm CW lasers were used for acquiring

the PL and Raman spectra of the material, respectively. The optical path for angle-resolved polarized Raman spectroscopy is schematically illustrated in Fig. S7a, wherein a half-wave plate is used to adjust the polarization of the incident laser beam. The laser power was kept below 1 mW in all measurements to avoid thermal damage. All measurements were performed under high vacuum within a Dewar flask to minimize environmental interference. Raman spectra were normalized to the silicon peak at 520.38 cm^{-1}.

2. Crystal Structure and Fundamental Photophysical Properties of 2DWP

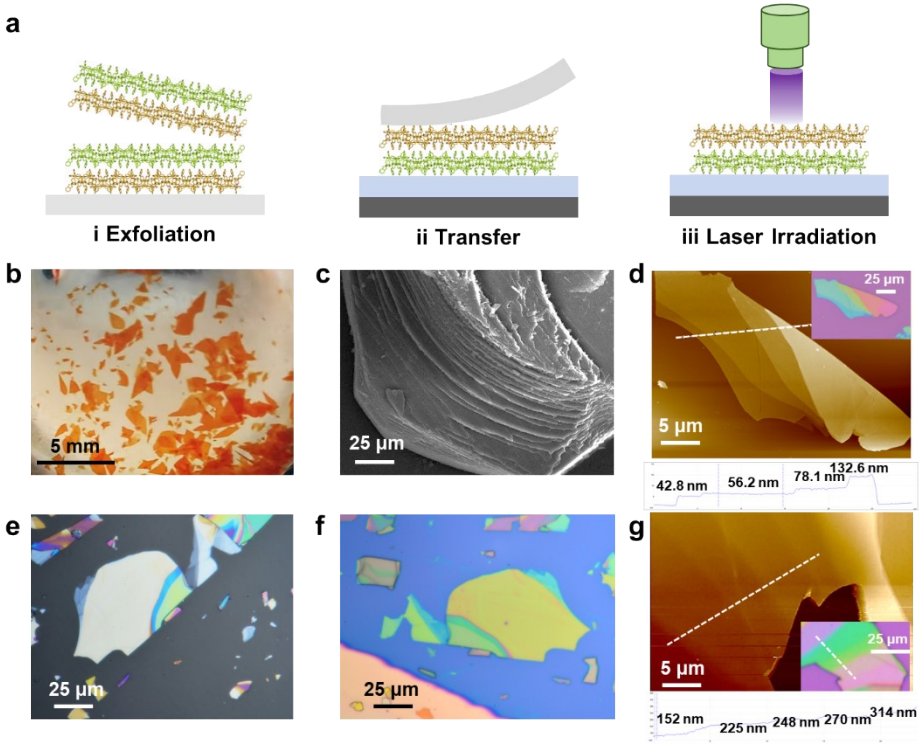

Fig. S1 Exfoliation and characterization of **2DWP** morphology and structure. **(a)** Exfoliation and transfer protocol for **2DWP** nanosheets. **(b)** Optical image of millimeter-scale **2DWP** single crystals. **(c)** SEM image of a **2DWP** crystal. **(d, g)** AFM images of exfoliated **2DWP** nanosheets with different thicknesses. **(e)** Optical image of **2DWP** nanosheets exfoliated onto a PDMS substrate. **(f)** Optical image of the same nanosheets after transfer onto a SiO_2/Si substrate.

As mentioned in the main text, mechanically exfoliated **2DWP** nanosheets were dry-transferred onto ~280 nm SiO_2/Si for optical excitation at selected wavelengths (Fig. S1a). Figure S1b shows millimeter-sized, orange-yellow **2DWP** single crystals. The layered stacking morphology of the crystal is confirmed by the SEM image (Fig. S1c). Mechanical exfoliation is employed to obtain **2DWP** nanosheets on a PDMS substrate (Fig. S1e), which are then transferred onto a ~280 nm SiO_2/Si substrate (Fig. S1f) for further characterization. The thicknesses of the obtained nanosheets are determined by AFM images (Figs. S1d,g) and their corresponding height profiles.

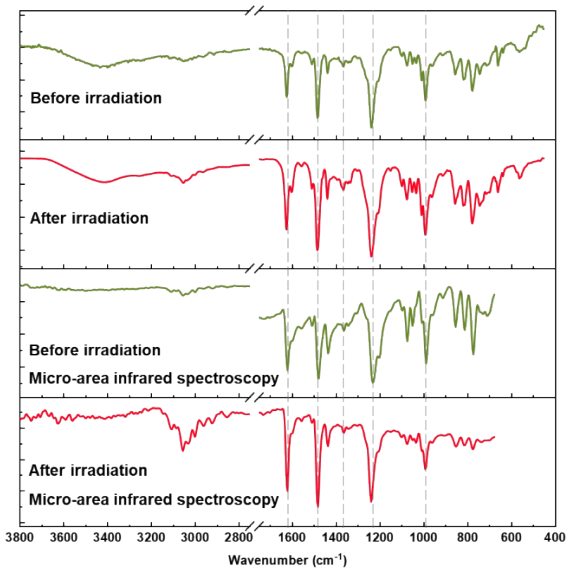

Fig. S2 Comparison of FTIR and micro-FTIR spectra of **2DWP** before and after photoirradiation.

Fig. S2 compares the chemical structure of **2DWP** before and after photoactivation using both FTIR and micro-FTIR spectroscopy. The high consistency of the characteristic peaks obtained by both techniques confirms that the molecular framework (including the dative B–N bonds and the aromatic backbone) remains intact during photoisomerization, with no evidence of covalent bond cleavage or side reactions.

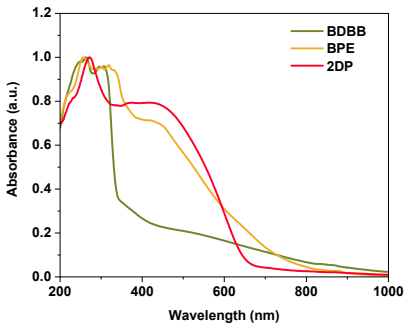

Fig. S3 UV–vis diffuse reflectance absorption spectra of **BDBB** and **BPE** monomers and **2DWP** crystals.

Fig. S3 compares the UV-Vis diffuse reflectance spectroscopy of the **BDBB** monomer, the **BPE** monomer, and the polymerized **2DWP** crystals. The absorption of the **BDBB** monomer is primarily confined to the UV region below 350 nm. In contrast, the absorption edge of the **BPE** monomer is significantly red-shifted, extending to approximately 700 nm in its solid (powder) state. For the polymerized **2DWP** crystals, the absorption edge remains around 600 nm, similar to that of the **BPE** monomer.

Notably, the absorption intensity in the 400–600 nm visible region is enhanced compared to the monomers. This observation indicates that the formation of the two-dimensional woven structure via B–N dative bonding not only establishes an extended conjugated framework but also introduces specific molecular packing motifs that enhance absorption at longer wavelengths.

3. Wavelength Selectivity in "Turn-On" Fluorescence

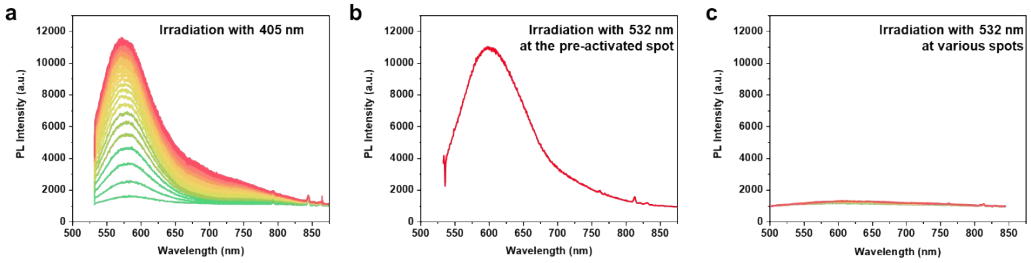

Fig. S4 Excitation-wavelength-dependent PL evolution. **(a)** Evolution of PL intensity of **2DWP** as a function of irradiation time under 405 nm excitation. **(b)** Corresponding PL evolution at the same spot shown in **(a)** (pre-activated by 405 nm) under 532 nm excitation. **(c)** PL evolution from various spots under 532 nm excitation.

Fig. S4 shows the evolution of the PL intensity of **2DWP** under different laser excitations. Upon 405 nm irradiation, the PL intensity increases markedly with time, exhibiting a characteristic emission peak around 575 nm (Fig. S4a). The peak intensity grows continuously and eventually saturates with prolonged irradiation. Subsequently, when the same pre-activated spot (from Fig. S4a) is excited in situ with a 532 nm laser, a significant fluorescence response is observed (Fig. S4b). In contrast, under direct 532 nm irradiation on pristine sample areas, the PL intensity remains extremely low across the entire spectral range and shows no significant change over time (Fig. S4c). This result clearly demonstrates the strongly wavelength-selective nature of the fluorescence "turn-on" response in **2DWP**.

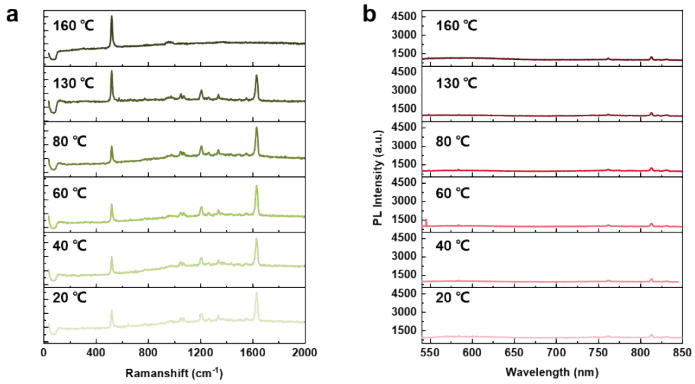

Fig. S5 Ruling out thermally induced degradation. **(a)** Temperature-dependent Raman spectra of **2DWP** measured from 20 to 160 °C. **(b)** Corresponding PL spectra collected from the same region over the temperature range of 20–160 °C under 532 nm excitation.

Fig. S5 presents a temperature-dependent spectroscopic study of **2DWP**. Fig. S5a shows the Raman spectra collected from 20 to 160 °C. All characteristic peaks remain discernible up to 130 °C, confirming the structural integrity of the material. The complete disappearance of Raman signals at 160 °C indicates material degradation. Fig. S5b shows the corresponding PL spectra acquired over the same temperature range. No significant PL emission is observed throughout the heating process prior to degradation. This result excludes the possibility that the observed fluorescence "turn-on" phenomenon originates from thermally induced structural degradation.

4. Lattice-Cooperative Response of the Woven Topology and Backbone Stability during Photoactivation

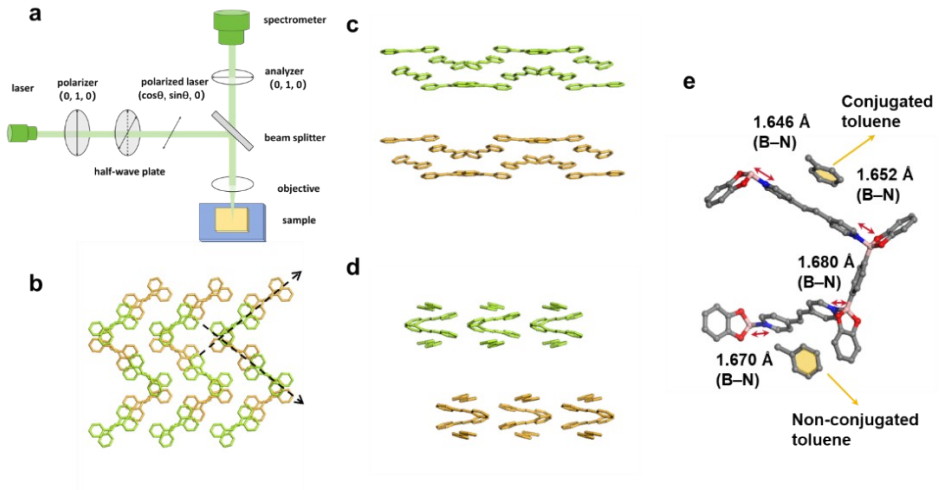

Fig. S6 Crystal packing and polarized Raman analysis. (**a**) optical path for angle-resolved polarized Raman spectroscopy. View of the crystal packing along the c-axis **(b)** b-axis **(c)** and a-axis **(d)** in bilayer **2DWP**. Solvent molecules, H atoms and **BDBB** were removed for a clear display of the relative positions of the **BPE** double bonds. **(e)** The interaction between solvent molecules (Conjugated and Non-conjugated toluene) and the lengths of dative B–N bonds.

Fig. S6 illustrates the crystal packing of bilayer **2DWP** viewed along the crystallographic c-axis (Fig. S6b), b-axis (Fig. S6c), and a-axis (Fig. S6d). Structural analysis reveals that the two layers are staggered, yet the principal axes defined by the alignment of **BPE** double bonds remain parallel in orientation between the layers. Importantly, within the same monolayer, these two sets of parallel axes (indicated by arrows in Fig. S6b) reside in two distinct chemical microenvironments due to differences in their specific coordination patterns with adjacent **BDBB** units and intralayer solvent molecules (Fig. S6e).

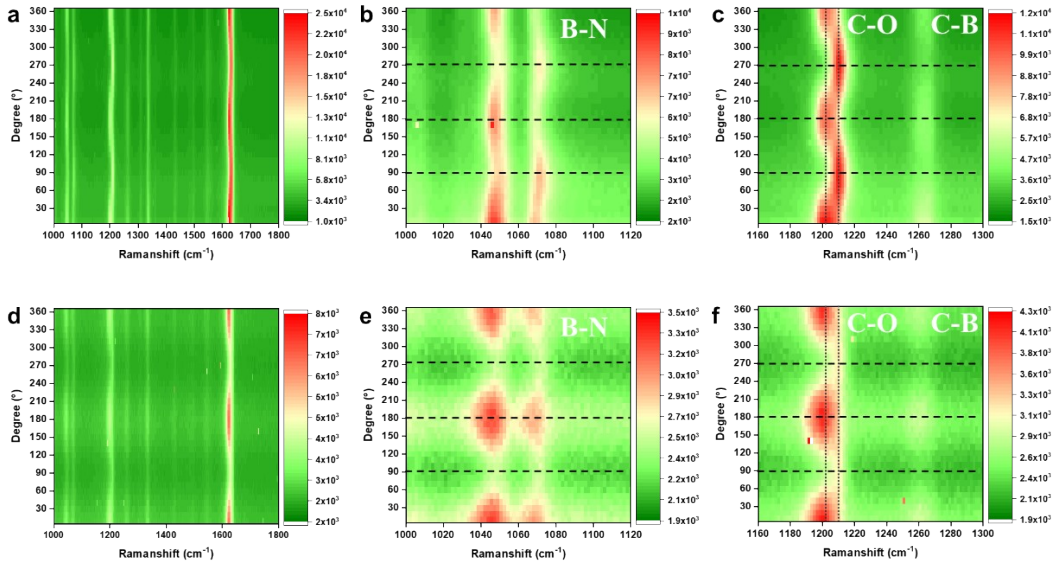

Fig. S7 Angle-resolved polarized Raman color maps of the changes in Raman peaks within the 1000-1800 cm^{-1} range before **(a)** and after **(d)** photoactivation (633 nm CW laser, 1 mW, spectrum acquisition time: 20 s). **(b, c)** and **(e, f)** particularly highlight the changes in the Raman peaks of the B-N bonds and C-O bonds before and after the light conversion process.

Figure S8 presents angle-resolved polarized Raman color maps in the 1000–1800 cm^{-1} region before and after photoactivation. Figs. S7a,d show the full spectral range, while (Figs. S7b,c) and (Figs. S7e,f) highlight the changes in the B–N and C–O/C–B bond regions, respectively. Similar to the C=C bonds discussed in the main text, the polarized Raman responses of B–N and C–O bonds also exhibit angle-dependent variations after irradiation. These results further support that the photoinduced configurational transformation propagates through the woven topology, affecting the anisotropic vibrational behavior of different chemical bonds across the lattice.

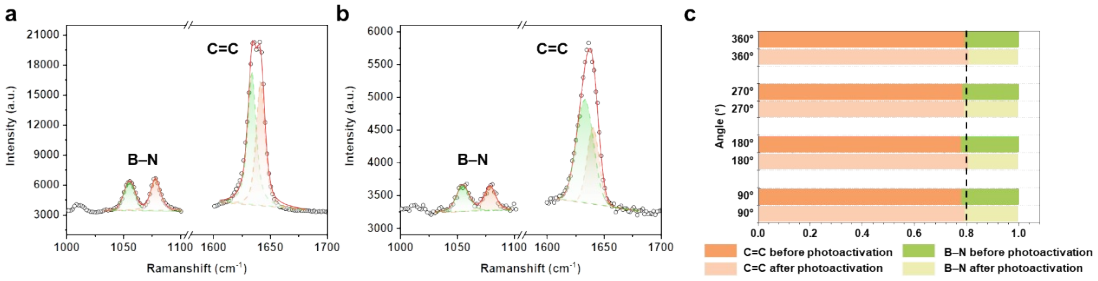

Fig. S8 Spectroscopic assessment of backbone integrity. **(a,b)** Peak fitting of the Raman spectra in the B–N stretching region (1040–1080 cm^{-1}) and the C=C stretching region (~1610–1650 cm^{-1}) before **(a)** and after **(b)** photoactivation. Solid lines represent the fitted components, while open circles denote the experimental data. **(c)** Relative intensity ratios of the C=C and B–N vibrational modes extracted from the fitting peaks at four polarization angles (90°, 180°, 270°, and 360°) before and after irradiation. The comparable C=C-to-B–N ratios across different orientations indicate that

photoactivation does not induce bond cleavage or backbone degradation.

Fig. S8 quantitatively assesses the integrity of the polymer backbone before and after photoactivation through Raman spectral fitting analysis. (Figs. S8a,b) show the peak fitting results in the B–N stretching region (1050–1080 cm^{-1}) and the C=C stretching region (1610–1650 cm^{-1}), respectively. The relative intensity ratios of the C=C to B–N vibrational modes, derived from the fitted peak areas at four polarization angles, are compared (Fig. S8c). The consistent ratios across different orientations before and after irradiation directly confirm that the covalent backbone of the polymer (both B–N and C=C bonds) remains intact during photoisomerization, with no bond cleavage or degradation.

5. Elucidating the Structural Origin of the Solid-State "Turn on" Fluorescence

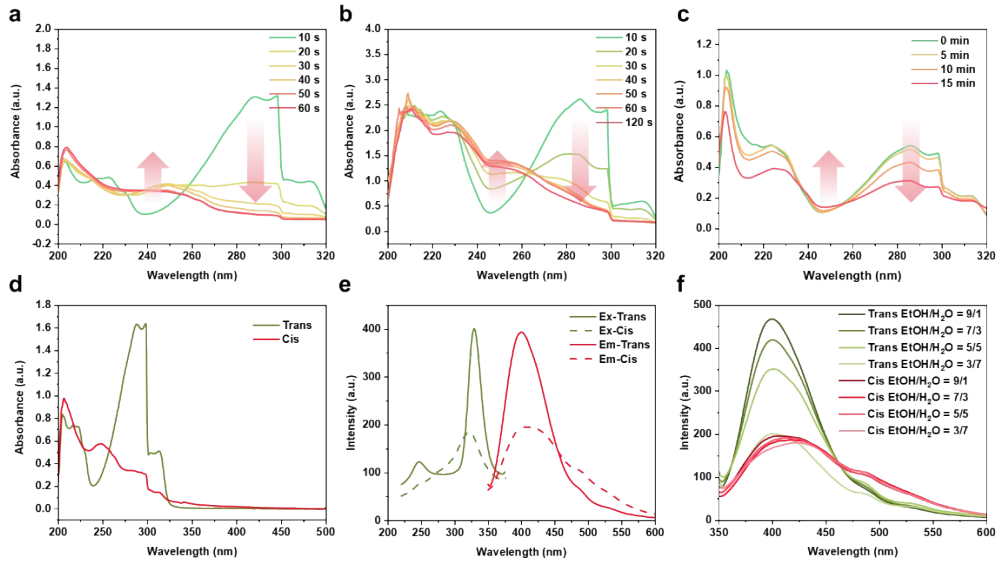

Fig. S9 Spectroscopic analysis of photoisomerization and aggregation effects. **(a)** Time-dependent UV–vis absorption spectra of **BPE** monomer in solution under continuous 295 nm irradiation. **(b)** Corresponding UV–vis absorption changes of **2DWP** dispersed in solution under identical 295 nm irradiation conditions. **(c)** UV–vis absorption spectra of photoactivated **2DWP** after 405 nm irradiation in the solid state. **(d)** Steady-state UV–vis absorption spectra of isolated *trans*- and *cis*-**BPE**. **(e)** Excitation and emission spectra of trans- and *cis*-**BPE** in dilute solution. **(f)** Emission spectra of trans- and *cis*-**BPE** measured in mixed ethanol/water solvents with increasing water fraction.

The supplementary spectroscopic data in Fig. S9 provide crucial molecular-level evidence supporting the proposed solid-state photoisomerization mechanism and fluorescence quenching behavior in the main text. As shown in Figs. S9a–c, the consistent spectral evolution exhibited by the **BPE** monomer in solution Figure S10a, **2DWP** in dispersion (Fig. S9b), and re-dissolved **2DWP** after solid-state photoactivation (Fig. S9c) collectively confirms that *trans*-to-*cis* isomerization occurs

within the **2DWP** crystals upon 405 nm irradiation. Figs. S9d–f further elucidate the relationship between stacking and emission at the molecular scale. The steady-state spectra of isolated *cis*- and *trans*-**BPE** monomers in dilute solution (Figs. S9d,e) reveal that the *cis*-isomer is inherently weakly fluorescent with a broad emission band. More critically, in ethanol/water mixtures with increasing water fraction (Fig. S9f), trans-**BPE** exhibits a pronounced aggregation-induced quenching (AIQ) effect, which is absent for *cis*-**BPE**. These results strongly underpin the conclusion in the main text: in the pristine **2DWP** crystal, the predominant, tightly stacked trans moieties undergo efficient AIQ due to strong π-π interactions, leading to a non-emissive state. Photoactivation converts a portion of the trans-**BPE** to the *cis*-**BPE**. The *cis*-**BPE** are not only weakly emissive themselves but, more importantly, their distorted geometry disrupts the original tight packing and mitigates the overall quenching effect. Consequently, the remaining, unconverted trans-**BPE** in the crystal become luminescent, manifesting as the macroscopic fluorescence "turn-on".

6. Semi-quantitative Estimation of the Apparent *Cis* Fraction

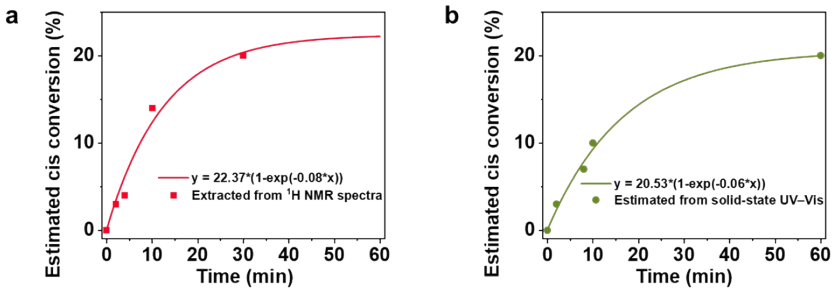

Fig. S10 Semi-quantitative estimation of the apparent *cis* fraction during photoisomerization in **2DWP**. **(a)** Estimated *cis* fraction extracted from the integrated area ratio of the $H^{c'}$ and H^{c} resonances in dissolved-state ^{1}H NMR spectra after irradiation. **(b)** Estimated *cis* fraction estimated from the integrated absorbance change in the 400–600 nm region of solid-state UV–Vis diffuse reflectance spectra during irradiation.

To provide a semi-quantitative evaluation of the solid-state photoisomerization process, the apparent *cis* fraction was independently estimated using two approaches. As shown in Fig. S10a, the *cis* conversion was extracted from the integrated area ratio of the H^{c} and $H^{c'}$ resonances in the dissolved-state ^{1}H NMR spectra after irradiation (Fig. 3c). Fig. S10b presents an independent estimation based on the evolution of the integrated absorbance in the 400–600 nm region of the solid-state UV–Vis diffuse reflectance spectra (Fig. 3b). The time-dependent conversion profiles were fitted using a pseudo-first-order saturation model:

$$y(t) = A(1 - e^{-kt})$$

Where A is the final *cis* conversion at the photostationary state, and the k is the apparent

rate constant.

Both methods yield comparable apparent photostationary *cis* fractions (~20–22%) and similar apparent rate constants, supporting the reliability of the estimated conversion and further corroborating the assignment of solid-state *trans–cis* photoisomerization in **2DWP**.

7. Cycling Stability of Wavelength-selective PL Switching

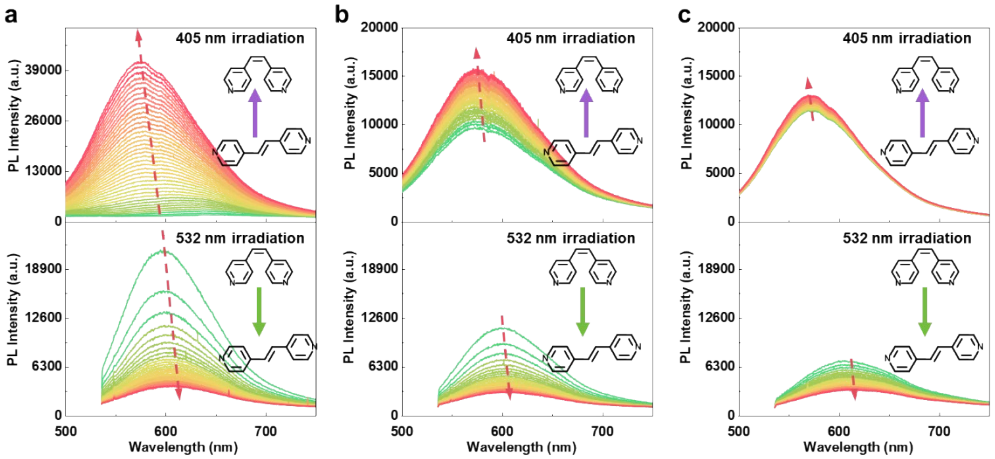

Fig. S11 Evaluation of fatigue resistance during repeated optical switching of **2DWP** (405/532 nm CW laser, excitation power: 50 μW; spectral integration time: 10 s per spectrum).

The PL spectral changes across three successive activation–deactivation cycles are illustrated in Figs. S11a–c. The upper panels show fluorescence enhancement under continuous 405 nm irradiation, while the lower panels show partial PL quenching under subsequent 532 nm irradiation. Although reversible modulation remains observable throughout the cycles, the switching amplitude gradually decreases with cycle number, indicating incomplete structural relaxation and accumulation of metastable configurations under topological constraints.

8. Additional Evidence for Topology-Mediated Fluorescence Activation

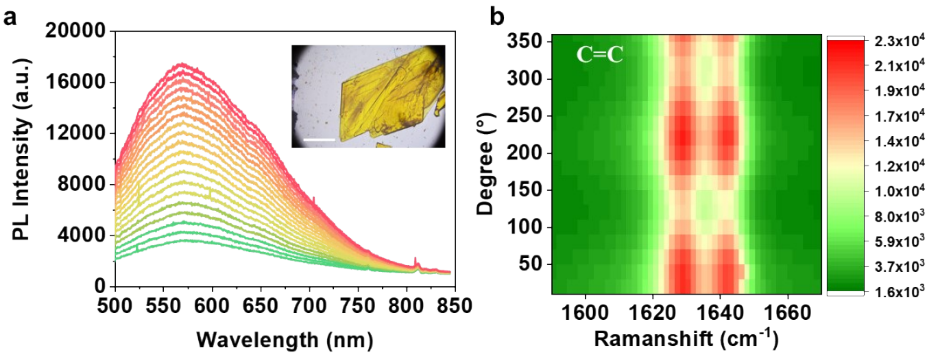

Fig. S12 Influence of solvent-derived packing environments on the photoresponse of 2D polymer crystals (**2DP-Mix**). **(a)** Time-dependent PL spectra of **2DP-Mix** crystals grown from mixed xylene under continuous 405 nm irradiation (405 nm CW laser, excitation power: 50 μW; spectral integration time: 10 s per spectrum)). **(b)** Angle-resolved polarized Raman mapping of the C=C stretching region for **2DP-Mix**.

An additional polymer crystal prepared using mixed xylene as the growth solvent (**2DP-Mix**) was investigated (Fig. S12). Although the altered solvent environment leads to noticeable differences in crystal appearance and polarization-dependent Raman features, indicative of modified local packing and chain orientation, a similar photoactivated fluorescence behavior remains observable under 405 nm irradiation. These observations suggest that the fluorescence activation is not uniquely associated with a specific guest solvent environment, but is instead governed primarily by photoisomerization within the woven polymer framework, with solvent-dependent packing acting as a secondary modulation factor.

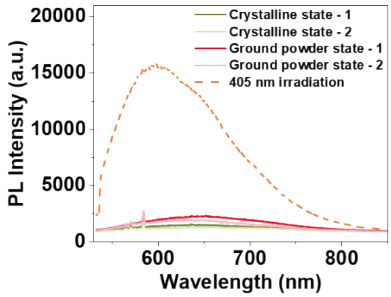

Fig. S13 Comparison of PL responses between crystalline and mechanically ground **2DWP** samples (532 nm CW laser, excitation power: 50 μW; spectral integration time: 10 s per spectrum).

Compared with the crystalline state, the ground powder exhibits only a weak increase in PL intensity. Two independent measurements are shown for each condition. These results indicate that partial disruption of intermolecular packing alone is insufficient to reproduce the photoactivated emissive state observed in **2DWP**.

9. Reference

[1] B. M. Rambo, J. J. Lavigne, "Defining Self-Assembling Linear Oligo(dioxaborole)s" *Chem. Mater.* **2007**, *19*, 3732–3739.

[2] D. Xiao, Z. Jin, G. Sheng, L. Chen, X. Xiao, T. Shan, J. Wang, R. Navik, J. Xu, L. Zhou, Q.-H. Guo, G. Li, Y. Zhu, J. F. Stoddart, F. Huang, "Single crystals of purely organic free-standing two-dimensional woven polymer networks" *Nat. Chem.* **2024**, *16*, 1906–1914.